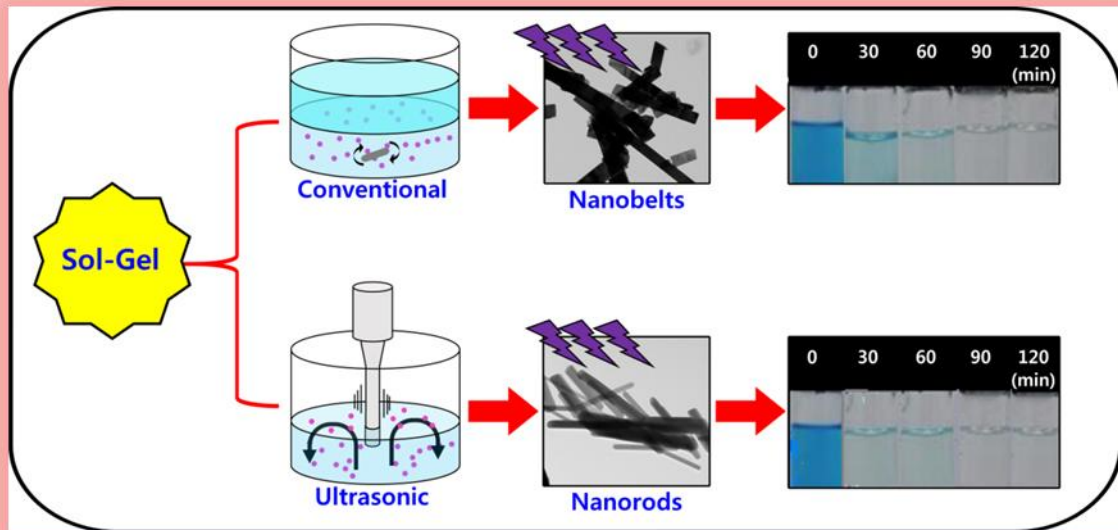# Chapter 5

Morphological evolution from 1-D to 2-D MoO$_3$ nanostructures via sol-gel for imparting rapid photocatalysis

"Observation is a passive science, experimentation an active science."

- Claude Bernard

5.1 Introduction

The influx of solar radiation on the earth surface presents opportunities of developing green processes which could be exploited to harness the solar energy for environmental remediation and energy applications. Photocatalysis is semiconductor catalyst enabled process transforming solar energy into chemical energy either for the production of hydrogen or degradation of harmful organic industrial chemicals such as dyes [1]. In the past decade, a significant number of nanocrystalline semiconductor metal oxides, such as TiO_2, ZnO, $LaCrO_3$, Cr_2O_3, SnO_2, MoO_3, have been utilized for photocatalytic dye degradation [2-7]. Among these nanostructured metal oxides, MoO_3, a wide band gap n-type semiconductor, is particularly interesting as, unlike most other intercalation transition metal oxides, it possesses an optical band gap that can directly harvest solar energy [8]. Additionally, it is photo-corrosion resistant and stable material. Owing to its typical properties, it has been explored for prospective applications in smart chromic systems, gas sensors, catalysts and energy storage [9-14]. However, it has not been routinely investigated as the photocatalytic material for dye degradation, and only sporadic reports are available in this direction [15]. To realize its practical application as industrial nano-photocatalyst, the key challenge is tunable–morphology oriented large scale synthesis using the facile yet scalable method.

In this context, we report a novel, the economical and hitherto unreported route to synthesize 1D (nanorod) and 2D (nanobelt) MoO_3 nanostructures at gram scale using conventional as well as sonochemical sol-gel technique. The details pertaining to the literature survey corresponding to the synthesis of MoO_3 nanostructures using various methods and a brief description of sol-gel route have already been presented in Chapter 2. The structural, morphological and optical properties of these structures were tuned by modifying the synthesis protocol. The photocatalytic properties of the resultant MoO_3 nanostructures were investigated for the degradation of the representative heteropolyaromatic pollutant dye, methylene blue (MB) in view of its extensive use in wide-ranging industrial applications. We have observed that appreciable photocatalytic MB dye-degradation can be accomplished within 30 minutes with high rate constants of 0.0786 min^{-1} and 0.233 min^{-1} for rod and belt-like MoO_3-nanostructures, respectively. The pilot results indicate that the resultant MoO_3 nano morphs can be potentially used as solar light-driven industrial photocatalyst material with inherent photostability. A brief comparison of the photocatalytic dye degradation studies in respected of the samples prepared by sol-gel method with two

representative nanocomposite samples develop ed by solid-solid reaction route is given at the end of chapter 5.

5.2 Molybdenum Oxide Nanostructures via Conventional and Ultrasonication Assisted Sol-Gel Route

5.2.1 Experimental:

5.2.1.1 Synthesis of MoO_3 nanostructures

Molybdenum oxide nanostructures were synthesized using conventional and sonochemical sol–gel method. In the conventional sol-gel method, ammonium molybdate powder (0.1 M) was dissolved in 50 ml of distilled water. Then urea (0.3 M) was added in 50 ml of distilled water. This solution was mixed with the previous solution. The mixture was subsequently stirred carefully using a magnetic stirrer, and acetic acid (75 ml) was simultaneously added dropwise to this solution. The solution was heated at 80 °C until the white colored suspension was formed in the solution. This suspension (sol) was allowed to settle (aged) for 8 days in order to form the sol-gel. The gel was dried at 100 °C in an oven for 6 h to obtain a white colored powder. Subsequently, this powder was heated at 400 °C in a furnace for 4 h which led to the formation of light blue colored powder. In sonochemistry assisted sol-gel method, the reaction procedure is similar to the conventional sol-gel method except that after the suspension was formed, it was irradiated using an ultrasonic horn for 2 h (with 'On' and 'Off' cycles of 5 sec, respectively). The resultant suspension was allowed to settle (aged) for 8 days to form the sol-gel. The gel was dried at 100 °C in an oven for 6 h to obtain a white colored powder. Subsequently, this powder was heated at 400 °C in a furnace for 4 h, and the off-white colored powder was finally obtained. The schematic showing conventional and sonochemical sol-gel process for nanomaterials synthesis is shown in figure 5.1.
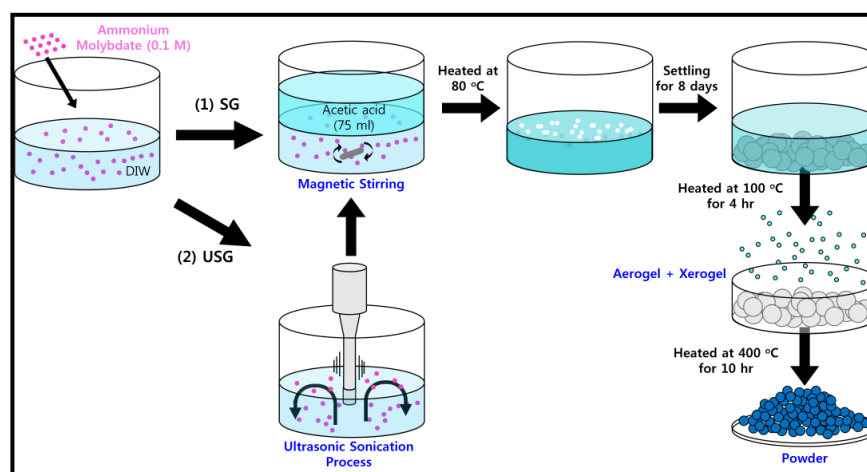

Figure 5.1 *Schematic depicting conventional and sonochemical sol-gel routes.*

The samples prepared using conventional and sonochemical sol-gel methods are referred as SG and USG, respectively.

5.2.1.2 Physico-chemical characterization

The structural information on virgin powder samples was obtained using X-ray diffraction (Bruker D8 Advance) technique. The diffracting angle $2(\theta)$ was varied between 10 - 80° range and the observed XRD peaks were compared with standard JCPDS cards. The surface morphological features of the samples were investigated by field emission scanning electron microscopy (FE-SEM) using HITACHI S-4800. The fine-scale microstructure of the samples was examined by field emission transmission electron microscopy (FE-TEM) using JEM-2200FS (JEOL, Japan) at an acceleration voltage of 200 KV. The samples for FETEM were prepared by dispersing fine powder of the resultant product in an isopropyl alcohol. A drop of dispersion was then transferred to carbon coated grid for further analysis. Diffuse reflectance UV-Visible absorbance spectra were recorded using Shimadzu UV-Vis-NIR spectrophotometer (Model UV-3600) over a wavelength range 300 to 800 nm.

5.2.1.3 Photocatalytic activity study

The preliminary results towards photocatalytic degradation were obtained by studying degradation of MB using the synthesized MoO_3 nanostructures. The photocatalytic activity of MoO_3 nanostructures was ascertained by carrying out the degradation of aqueous MB solution under 400 W mercury vapor lamp irradiation. The catalyst powder consisting of nanostructured MoO_3 (50 mg) was suspended in 100 ml aqueous MB solution (10 ppm, pH 7) in a 250 ml conical flask and stirred for 30 min in the dark, at room temperature. Then, the mixture was continuously stirred under 400 W mercury vapor lamp. At regular intervals of time, aliquots of aqueous solution were taken from the flask, centrifuged and the UV–vis absorption spectrum of the clear solution was recorded using a double beam spectrophotometer. The decrease in the absorbance (C/C_t) value at 664 nm wavelength which corresponds to the signature peak of the absorption spectrum of MB was employed to determine the extent of degradation of MB with respect to the irradiation time.

5.2.2 Results and discussion

5.2.2.1 X-ray diffraction

Typical XRD patterns of the as-prepared products obtained using conventional and sonochemical sol-gel method are presented in figure 5.2. Both the XRD patterns predominantly show peaks arising from reflections of orthorhombic α-MoO_3 (JCPDS #05-0508) at 2θ ~12.81, 23.51, 25.81, 27.45,

29.60, 33.82, 35.70, 39.31, 45.91, 49.55, 53.14, 55.63, 56.43, 58.92, and 64.74° corresponding to planes (020), (110), (040), (021), (130), (101), (041), (150), (200), (002), (211), (112), (042), (081) and (062), respectively. Both the samples exhibit sharp peaks ascribable to their highly crystalline nature. However, relatively sharper peaks in the case of SG sample imply its better crystallinity.
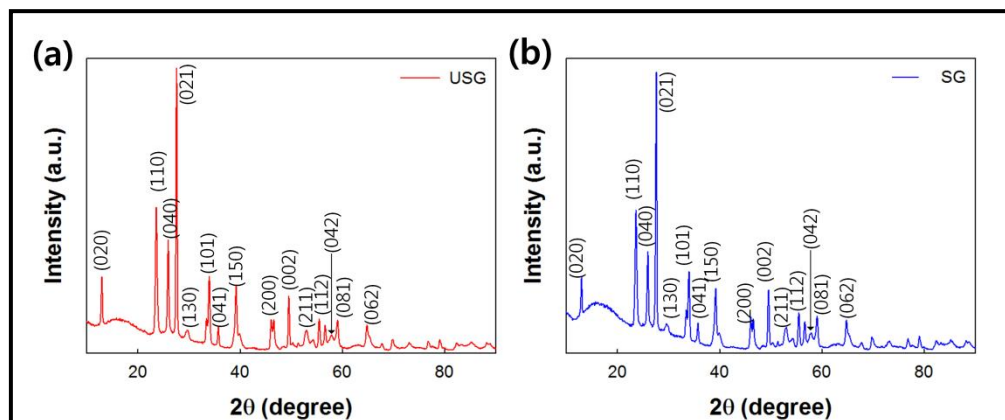

Figure 5.2 *XRD patterns of resultant product samples (a) USG and (b) SG, respectively.*

5.2.2.2 Field emission scanning electron microscopy and field emission transmission electron microscopy

Typical FESEM and FETEM images of the sample prepared using conventional sol-gel method are displayed in figure 5.3. FESEM image clearly discloses the formation of sheet-like nanostructures having a thickness of ~ 50 nm (figure 5.3a). Low magnification FETEM image for the sample SG (figure 5.3b) discloses the formation of sheet/belt-like nanostructures having a width of 200-500 nm and length running from 1 μm to 4 μm. High magnification image shows the formation of sheet-like structures which are few nanometer thick (figure 5.3c). The lattice image presented in figure 5.3d indicates long-range crystalline nature of the sample having d value of 3.30 Å which matches with the (021) plane. The SAED pattern of SG sample (inset of figure 5.3c) shows the presence of regular bright spots with d values corresponding to planes (110), (040), (021) and (101), respectively. The origin of these regular spots may be attributable to the long range crystalline nature of the sample. The SAED pattern of a single MoO_3 nanobelt (figure 5.3c) reveals that nanobelts grow in the [101] direction and their wide facet correspond to (021) crystalline plane of MoO_3. These results differ from the results obtained by other

researchers [16-18] where prominent growth along anisotropic [0 *l* 0] (where, *l* = 2, 4, 6, etc) direction was obtained.
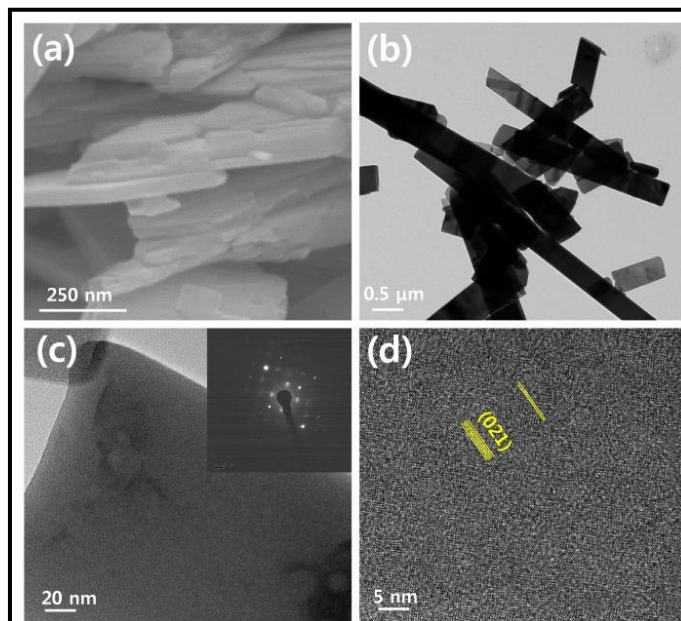

Figure 5.3 *Electron microscopy images of the SG sample (a) FESEM image; FETEM images corresponding to (b) low magnification (inset SAED), (c) high magnification and (d) lattice image.*

FESEM image of USG samples reveals the formation of 1D nanorods instead of 2D sheet -like structures (figure 5.4a). The length of these nanorods is in the range of 200 nm to 1 µm while the thickness varies from 50-150 nm. The low magnification FETEM image corresponding to sample USG (figure 5.4b) displays formation of 1D nanorods-like structures. The length of such nanorods is 500 nm-1.5 µm and width falls in the broad range of 40-150 nm. However, most of the nanorods have a width in the range of 40-80 nm. These results corroborate well with the FE-SEM data. The high magnification image (figure 5.4c) reveals two representative nanorods having blunt edges and thickness of 40 nm and 100 nm each. The lattice image is shown in figure 5.4d suggests polycrystalline nature of the nanorods having different crystallite orientation along (110), (040), (021) and (130), respectively. The SAED pattern of USG sample (figure 5.4c) comprise rings made by spots arising from (110), (040), (021), (101), (111) reflections. It typically implies presences of polycrystalline nano-grains which constitute the nanorods.
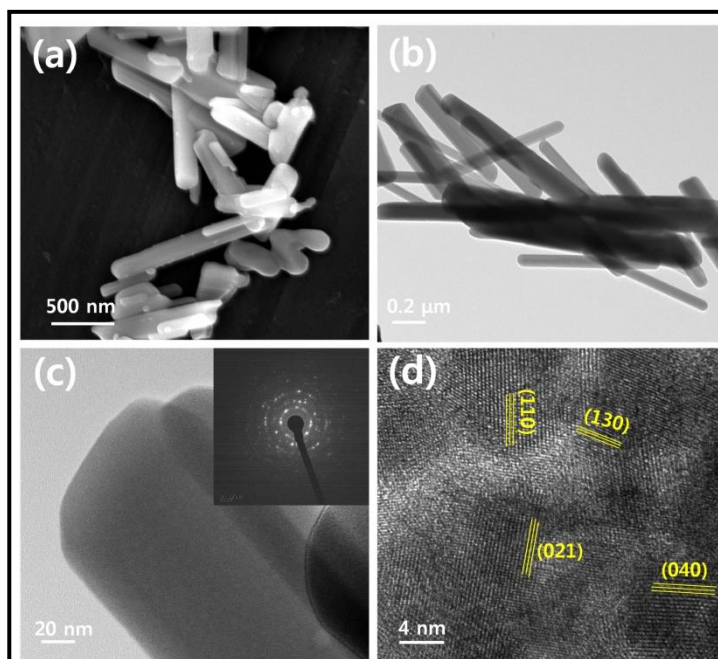
Figure 5.4 *Electron microscopy images of the USG sample (a) FE-SEM image; FE-TEM images corresponding to (b) low magnification (inset SAED), (c) high magnification and (d) lattice image.*

5.2.2.3 UV-vis spectroscopy

UV-vis spectra of MoO_3 samples are presented in figure 5.5. Both the SG and USG samples exhibited a strong absorption band between 250 and 400 nm in the UV range which may be attributed to the charge transfer of the Mo-O band in the MoO_6^{6-} octahedron [19, 20].
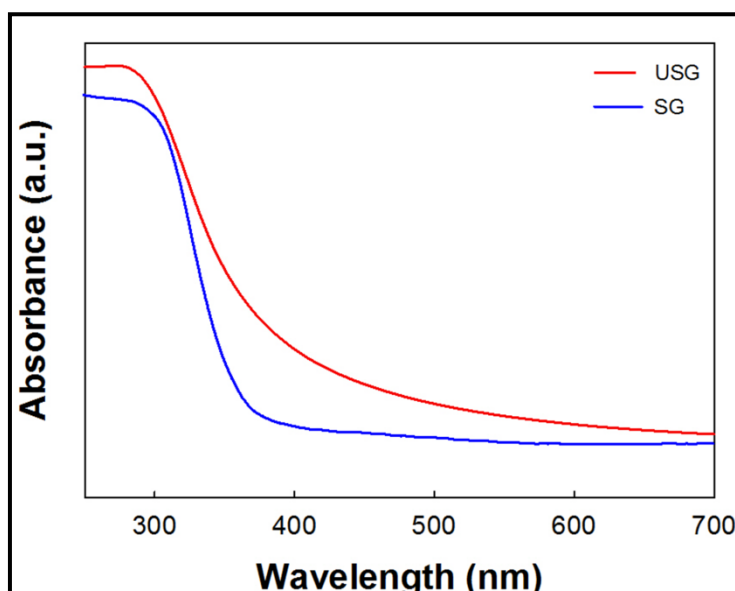

Figure 5.5 *UV-vis spectra of SG and USG samples.*

The sample prepared using the conventional sol-gel technique (SG) displays very sharp absorption at ~ 360 nm. However, for USG sample, the absorption edge is not very sharp even though it is in the same range as that of SG. The corresponding band gaps calculated for these samples are found to be 3.3 eV and 3.04 eV, respectively. The obtained band gap values are higher than the reported band gap value of bulk MoO_3 which can be attributed to the quantum size effect [21]. Nevertheless, the absorption of USG sample extends to the visible region, which may be due to the presence of nanocrystalline gains induced defects in the sample.

5.2.2.4 Growth mechanism

α-MoO_3 possesses an orthorhombic structure belonging to the space group P_{bnm} (D^{16}_{2h}) [22] and has a unique layered structure where distorted MoO_6 octahedrons share both edges (along [001] direction) and corners (along [1 0 0] direction). The double layers of MoO_6 octahedra are held together by two different bonds—covalent bonds in the *a*- and *c*-axes, i.e. along (*h* 0 0) and (0 0 *l*) [23]. The interactions between layers along b axis i.e. the (0 *k* 0) direction are due to weak Van der Waals forces. From the energy viewpoint, the corresponding energy released along [0 0 1] is much greater than that of along [1 0 0] direction [17]. Planar growth rates along axes of the crystal have the following sequence {0 0 1} > {1 0 0} > {0 1 0}, [24] so the nanoribbons which grow along [0 0 1] direction are much favored. In most of the cases, the nanorod or nanobelt structures have been reported when the anisotropic growth along (0 *k* 0) planes takes place [15, 21, 24, 25]. However, isotropic growth also may lead to nanorod and nanobelt-like structures owing to inherent unique layered structure of MoO_3 [19, 26]. There is some controversy associated with whether the co-ordination of chains forming MoO_3 is six-fold (MoO_6 octahedrons) or four-fold (MoO_4 tetrahedron) [27]. Nonetheless, many studies have confirmed the existence of MoO_3 with six-fold coordination which might seemingly occur in the present case also [28, 29]. As far as the reaction is concerned, ammonium molybdate is the source of molybdenum as well as NH_4^+ ions, urea helps in the oxidation and provide NH_4^+ ions in water. Acetic acid plays a very important role as a stabilizer of the sol. During the nucleation and growth process, NH_4^+ and OH^- ions play a very crucial role in shaping the morphology of the final product. Mo species spontaneously react with oxygen at the supersaturation point to form MoO_6 octahedral units where each central molybdenum atom is surrounded by octahedrally co-ordinated

six oxygen atoms and form the basic building blocks of MoO_3 particles. These nascent octahedral crystal nuclei grow and self-assemble to form many tiny crystalline MoO_3 nuclei by a diffusion mechanism in the reacting solution when it reaches its solubility limit [30]. In sol-gel method, isotropic growth is expected to own to longer reaction time which results in slow growth and the growth is governed by NH_4^+ and OH^- ions. This is the case for the conventional sol-gel method. However, in the case of sonochemical assisted sol-gel method, even though the isotropic growth takes place, acoustic cavitation provides sufficient energy for the nuclei to orient themselves for the growth to take place which are not planar, i.e., instead of planar (2D) sheet-like structures, rod-like 1D structures grow. Thus, even though all reaction conditions are the same, the final products formed by conventional and sonochemical assisted sol-gel method can possess different morphologies. When the dried gels are heated to high temperatures of 400 ^{0}C, removal of ammonia and dehydration process takes place and morphological isotropic transition from a 2D nanobelt to 1D nanorod can be clearly realized (as illustrated in figure 5.6) for the MoO_3 nanostructures prepared by conventional and sonochemical assisted sol-gel method, respectively.
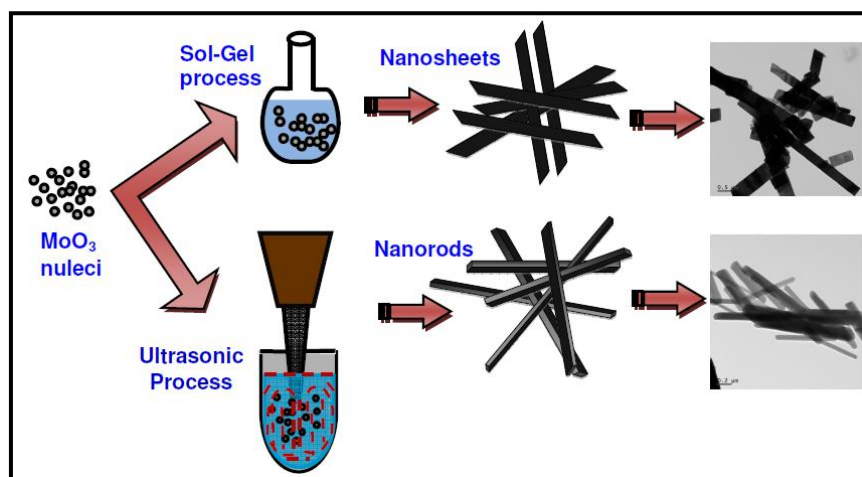

Figure 5.6 *Growth mechanism for MoO₃ nanostructures - SG and USG, respectively.*

Even though XRDs of the samples prepared by the conventional and sonochemical assisted sol-gel method are the same, their morphological features exhibit a transition from 2D nanobelt to 1D nanorod-like features. Manivel et al. and Jin et al. have postulated that sonochemical reactions arising from acoustic cavitation phenomena might be responsible for the formation of relatively smaller sonochemically grown MoO_3 nanostructures [31, 32]. In our case, we also believe that the acoustic cavitation might have

provided the energy required to evolve 1D growth of the crystallites, unlike 2D growth as observed in the case of a conventional sol-gel reaction.

It is quite interesting to note that although crystalline phase (structural) transition cannot occur by switching synthesis technique from conventional to sonochemical assisted sol-gel, it impacts change in morphology of the resultant nanostructures, which can critically influence their effective surface area and, in turn, grant a potential avenue for catalytic reaction to take place.

5.2.3 Solar-light driven photo-catalytic activity

The photocatalytic degradation of methylene blue solution using MoO_3 photocatalyst as a function of irradiation time is shown in figure 5.7. When SG and USG samples were subjected to degradation of MB dye in aqueous solution under UV light illumination, each one exhibited specific photocatalytic properties. As the irradiation time is increased, appreciable fading in the of color of the solution from dark blue to lighter one is photographically illustrated in figure 5.7 (a) and (b) for SG and USG samples, respectively. The absorption spectrum of pristine MB presented in figure 5.7 designates strong absorption band centered at 665 nm with a shoulder around 610 nm typically associated with monomeric and dimeric forms of MB, respectively [30]. The rapid decrease in the intensity of characteristic MB absorption peaks (which signifies lesser degradation time) was noticed for such nanostructured MoO_3 mediated photocatalytic degradation (figure 5.7 (c) and (d)).
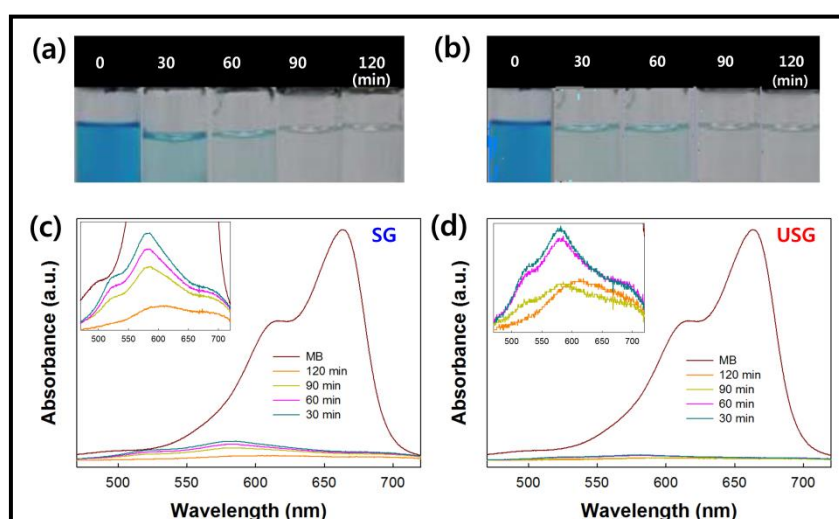

Figure 5.7 *(a & b) Photo images and (c & d) absorption spectra of MB solution in the presence of MoO_3 nanostructure at different time intervals for SG and USG samples, respectively.*

Degradation of dye and its rate constant (C) are calculated by using the equations 1& 2:

$$\text{\% degradation of dye} = A_0\text{-}A/A_0 \times 100 \qquad (1)$$

$$\ln(C_0/C_t) = k_{obs}C \qquad (2)$$

Where A_0 and A are the initial absorbance and absorbance at time 't' of the dye, while C_0 and C_t are initial concentration and concentration in the bulk solution at time 't', respectively and t the reaction time while, k_{obs} is the observed rate constant. Quite surprisingly, both the samples have exhibited excellent and expeditious MB degradation i.e. more than 90% within 30 min as evidenced in figure 5.8a. Interestingly, SG sample degrades more than 97.5% MB solution while USG sample degrades nearly 90% MB solution during this time-span. Complete degradation of dye occurred within 90 min of UV irradiation for both the samples. The rate constant follows apparent pseudo-first-order kinetic behavior and k_{obs} values for USG and SG samples are 0.0786 min^{-1} and 0.233 min^{-1}, respectively, as estimated from the plots of figure 5.8b. The better rate constant corresponding to SG sample can be attributed to its 2D nanobelt morphology which presumably enhances the relative density of photocatalytic centers. Nevertheless, the results indicate that both the types of MoO$_3$ nanomorphs can act as good photocatalyst in the dye-degradation reaction for solar energy enabled environmental remediation.
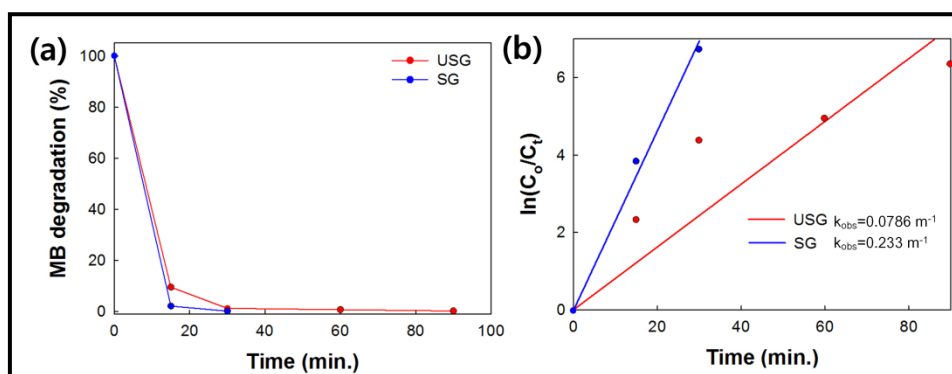

Figure 5.8 Plots of (a) % MB degradation and (b) photocatalytic chemical kinetics corresponding to SG and USG samples.

The typical mechanism of photocatalytic MB degradation is presented in figure 5.9.

When the solution containing the photocatalyst (MoO$_3$) and MB is illuminated using mercury vapor lamp, the valence band (VB) electrons get excited into the conduction band (CB) producing electron–hole (e$^-$ - h$^+$) pairs.

An efficient separation and swift transport of the photo induced charge carriers towards the catalytic surface facilitates oxidation-reduction reactions.
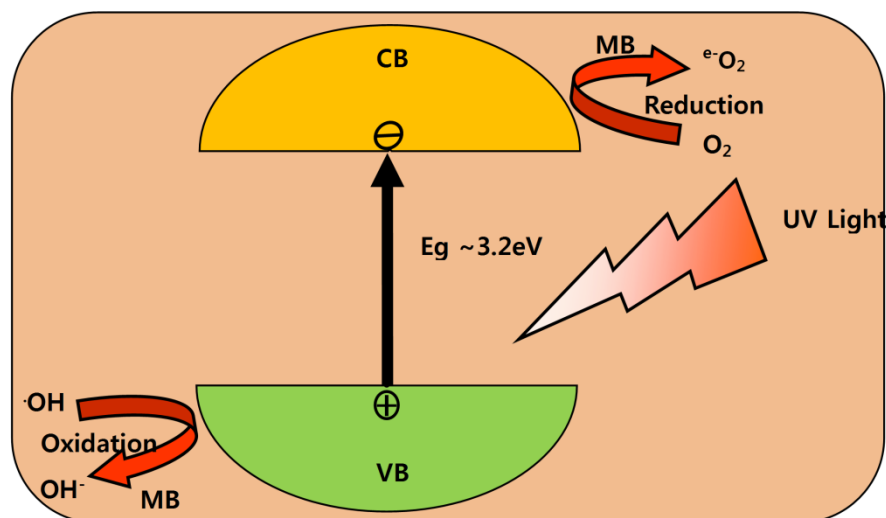

Figure 5.9 *Mechanism for photocatalytic activity of MoO$_3$ nanostructures.*

Thus, the oxidation of photo induced holes and surface bound H$_2$O and OH$^-$ produce the hydroxyl radical species, while, a reduction between photo induced electrons and adsorbed oxygen creates superoxide anion radicals. These two radicals are reported to be the factor accountable for MB degradation [30, 33, 34].

5.2.4 Comparison of MB dye degradation for samples prepared by different routes

Time (min)	Solid-Solid State		Sol-Gel	
	Sample 1	Sample 2	SG	USG
30	x	x	√	√
60	x	x	√	√
90	x	x	√	√
120	x	x	√	√

Table 5.1 *Comparison and MB dye degradation % of nanostructures samples using solid-solid route.*

Photocatalytic dye-degradation results against MB for MoO_3 powders prepared by solid-solid-state routes against conventional and ultrasonic sol-gel routes given in Table 5.1. Samples prepared using solid-solid state route exhibited no dye degradation effect. The reason for poor photocatalytic dye degradation for samples prepared in solid-solid state route is quite obvious as nanostructures are capped by a thick layer of highly insulating polymer i.e. PPS which prevents the effective charge transfer.

5.5   Summary

We have successfully demonstrated that morphological (isotropic) transition from 2D nanobelt to 1D nanorod can be clearly realized in the case of orthorhombic MoO_3 nanostructures prepared by conventional and sonochemistry assisted sol-gel method, respectively. The sample prepared by the conventional sol-gel method has exhibited long range crystalline order. The band gap values are estimated to be 3.3 eV and 3.04 eV, respectively for the nanostructured samples generated by conventional and sonochemistry assisted sol-gel methods. The resultant MoO_3 nanomorphs were used as a photocatalyst to degrade MB solution. Rate constants for the nanorod-like and nanobelt-like samples of MoO_3 were observed to be 0.0786 m^{-1} and 0.233 m^{-1}, respectively. Swift degradation of MB within very short irradiation time of 30 minutes implies that sol-gel produced orthorhombic α-MoO_3 nanostructures are the promising candidates for the photo degradation of organic dyes ensuing environmental remediation. Nevertheless, the photocatalytic performance needs to be judged with respect to the role and the subsequent optimization of various experimental parameters such as catalyst concentration, dye concentration, light flux intensity and operating temperature. Our efforts in this direction are in progress.

Reference

[1] Madhavan J., Kumar, Anandan P. S., Zhou M., Grieser F. and Kumar A. (2010) "Ultrasound assisted photocatalytic degradation of diclofenac in an aqueous environment" *Chemosphere* 80:747–752.

[2] Kasuga T., Hiramatsu M., Hoson A., Sekino T. and Niihara K. (1999) "Titania nanotubes prepared by chemical processing" *Adv. Mater.* 11: 1307–1311.

[3] Zach M. P., Ng K. H. and Penner R. M. (2000) "Molybdenum nanowires by electrodeposition" *Science* 290:2120-2123.

[4] Lota G., Frackowiak E., Mittal J. and Monthioux M. (2007) "High performance supercapacitor from chromium oxide-nanotubes based electrodes" *Chem. Phys. Lett.* 434**:**73-77.

[5] Xinyu Z., Jiaqian Q., Yanan X., Pengfei Y., Bing Z., Limin W. and R. Liu. (2014) "Effect of aspect ratio and surface defects on the photocatalytic activity of ZnO nanorods" *Scientific Reports* 4:4596 (1-8).

[6] Jose J., Ameta J. and Punjabi P. B. (2007) "Lanthnaum chromite oxide catalyst: synthesis, characterization and photocatalytic activity shown in Azure-B Ameta" *Bull. Catal. Soc. Ind.* 6: 110-118.

[7] Gambhire A. B., Lande M. K., Kalokhe S. B., Shirsat M. D., Patil K. R., Gholap R. S. and Arbad B. R. (2008) "Synthesis and characterization of high surface area CeO_2 doped SnO_2 nanomaterial" *Mater. Chem. Phys.* 112: 719-722.

[8] Lou N. S., Yap N., Scott J., Amal R. and Ng Y. H. (2014) "Influence of MoO_3 (110) crystalline plane on its self-charging photoelectron-chemical properties" *Scientific Reports* 4: 7428.

[9] He T. and Yao J. (2006) "Photochromism in composite and hybrid materials based on transition-metal oxides and polyoxometalates" *Prog. Mater. Sci.* 51: 810–879.

[10] Yang S., Wang Z., Hu Y., Luo X., Lei J., Zhou D., Fei L., Wang Y. and Gu H. (2015) "Highly responsive room-temperature hydrogen sensing of α-MoO_3 nanoribbon membranes" *ACS. Appl. Mater. Interf.* 7: 9247−9253.

[11] Manal A., Sivacarendran B., Matthew F., Kay L., Wojtek W., Jian O. and Kourosh Z. (2014) "Two dimensional α-MoO_3 nanoflakes obtained using solvent-assisted grinding and sonication method: application for H_2 gas sensing" *Sensors and Actuators B* 192: 196–204.

[12] Malakooti, Shafie S., Hosseinabadi R., Heravi M., Zakeri M. and Mohammadi N. (2014) "MoO_3 nanoparticles synthesis via hydro-solvothermal technique and Its

application as catalyst for efficient ring opening of epoxides with amines under solvent-free conditions" *Chemistry* 44: 1401-1406.

[13] Zhiyu W., Srinivasan M. , Xiong W. D. and Lou (2012) "Ultralong α-MoO$_3$ nanobelts: synthesis and effect of binder choice on their lithium storage properties" *J. Phys. Chem. C.* 116:12508−12513.

[14] Chang J., Jin M., Yao F., Kim T. H., Le V. T., Yue H., Gunes F., Li B., Ghosh A., Xie S. and Lee Y. H. (2013) "Asymmetric supercapacitors based on graphene/MnO$_2$ nanospheres and graphene/MoO$_3$ nanosheets with high energy density" *Adv. Funct. Mater.* 23: 5074–5083.

[15] Chen Y., Lu C., Xu L., Ma Y., Hou W. and Zhu J. J. (2010) "Single-crystalline orthorhombic molybdenum oxide nanobelts: synthesis and photocatalytic properties" *Cryst. Eng. Comm.* 12:3740–3747.

[16] Li X. L., Liu J. F. and Li Y. D. (2002) "Low-temperature synthesis of large-scale single-crystal molybdenum trioxide (MoO$_3$) nanobelts" *Appl. Phys. Lett.* 81: 4832- 4834.

[17] Li Y. B., Bando Y., Golberg D. and Kurashima K. (2002) "Field emission from MoO$_3$ nanobelts" *Appl. Phys. Lett.* 81: 5048-5050.

[18] Chen X., Lei W., Liu D., Hao J., Cui Q. and Zou G. (2009) "Synthesis and characterization of hexagonal and truncated hexagonal shaped MoO$_3$ nanoplates" *J. Phys. Chem. C.* 113: 21582-21585.

[19] Tian X., Qin L., Xiangdong L., Jian M. and Xueqiang C. (2006) "Morphology-controllable synthesis and characterization of single-crystal molybdenum trioxide" *J. Phys. Chem. B* 110: 2006-2012.

[20] Neeraj S., Kijima N. and Cheetham A. K. (2004) "Novel red phosphors for solid-state lighting: the system NaM (WO$_4$)$_{2-x}$(MoO$_4$)x:Eu^{3+}" *Chem. Phys. Lett.* 387: 2-6.

[21] Cheng L., Shao M., Wang X. and Hu H. (2009) "Single-crystalline molybdenum trioxide nanoribbons: photocatalytic, photoconductive, and electrochemical properties" *Chem. Eur. J.* 15: 2310 – 2316.

[22] Ding Q. P., Huang H. B., Duan J. H., Gong J. F., Yang S. G., Zhao X. Z. and Du Y. W. (2006) "Molybdenum trioxide nanostructures prepared by thermal oxidization of molybdenum" *J. Cryst. Growth* 294: 304 – 308.

[23] Navas I., Vinodkumar R., Lethy K. J., Detty A. P., Ganesan V., Sathe V. and Pillai M. (2009) "Growth and characterization of molybdenum oxide nanorods by RF magnetron sputtering and subsequent annealing" *J. Phys. D: Appl. Phys.* 42: 175305(1-8)**.**

[24] Zeng H. C. (1998) "Vapour phase growth of orthorhombic molybdenum trioxide crystals at normal pressure of purified air" *J. Cryst. Growth* 186: 393 – 402.

[25] Sivakumar R., Gopalakrishnan R., Jayachandran M. and Sanjeeviraja C. (2007) "Characterization on electron beam evaporated α-MoO$_3$ thin films by the influence of substrate temperature" *Curr. Appl. Phys.* 7: 51-59.

[26] Hu X. K., Qian Y. T., Song Z. T., Huang J. R., Cao R. and Xiao J. Q. (2008) "Comparative study on MoO$_3$ and H$_x$MoO$_3$ nanobelts: structure and electric transport" *Chem. Mater.* 20: 1527–1533.

[27] Dieterle M., Weinberg G. and Mestl G. (2002) "Raman spectroscopy of molybdenum oxides Part I. structural characterization of oxygen defects in MoO$_{3-x}$ by DR UV/VIS, raman spectroscopy and x-ray diffraction" *Phys. Chem. Chem. Phys.* 4: 812–821.

[28] Labanowska M. (1999) "Paramagnetic defects in MoO$_3$—revisited" *Phys. Chem. Chem. Phys.* 1:5385-5392.

[29] Mestl G., Verbruggen N. F. and Knoezinger H. (1995) "Mechanically activated MoO$_{3.2}$. characterization of defect structures" Langmuir 11:3035- 3041.

[30] Chithambararaj A., Sanjini N. S., Velmathi S. and Bose A. C. (2013) "Preparation of *h*-MoO$_3$ and *α*-MoO$_3$ nanocrystals: comparative study on photocatalytic degradation of methylene blue under visible light irradiation" *Phys. Chem. Chem. Phys.* 15:14761-14769.

[31] Manivel A., Lee G. J., Chen C. Y., Chen J. H., Ma S. H., Horng T. L. and Wu J. J. (2015) "Synthesis of MoO$_3$ nanoparticles for azo dye degradation by catalytic ozonation" *Mater. Res. Bull.* 62:184–191.

[32] Jin B., Bang H. and Suslick K. S. (2010) "Applications of ultrasound to the synthesis of nanostructured materials" *Adv. Mater.* 22:1039-1059.

[33] Arbuj S. S., Hawaldar R. R., Varma S., Waghmode S. B. and Wani B. N. (2012) "Synthesis and characterization of ATiO$_3$ (A= Ca, Sr and Ba) perovskites and their photocatalytic activity under solar irradiation" *Sci. Adv. Mater.* 4:568-572.

[34] Meshram S. P., Adhyapak P. V., Mulik U. P. and Amalnerkar D. P. (2012) "Facile synthesis of CuO nanomorphs and their morphology dependent sunlight driven photocatalytic properties" *Chem. Engg. J.* 204: 158–168.